Published as: Derluyn, H., Dewanckele, J., Boone, M.N., Cnudde, V., Derome, D., Carmeliet, J. 2014. Crystallization of hydrated and anhydrous salts in porous limestone resolved by synchrotron X-ray microtomography, *Nuclear Instruments and Methods in Physics Research B*, in press. DOI: 10.1016/j.nimb.2013.08.065.

CRYSTALLIZATION OF HYDRATED AND ANHYDROUS SALTS IN POROUS LIMESTONE RESOLVED BY SYNCHROTRON X-RAY MICROTOMOGRAPHY

Hannelore Derluyn[1,2,3,*], Jan Dewanckele[3], Matthieu N. Boone[4], Veerle Cnudde[3], Dominique Derome[2] and Jan Carmeliet[1,2]

[1]ETH Zurich, Chair of Building Physics, Wolfgang-Pauli-Strasse 15, 8093 Zürich Hönggerberg, Switzerland, email: carmeliet@arch.ethz.ch

[2]EMPA, Swiss Federal Laboratories for Materials Science and Technology, Laboratory for Building Science and Technology, Überlandstrasse 129, 8600 Dübendorf, Switzerland, email: dominique.derome@empa.ch; jan.carmeliet@empa.ch

[3]Ghent University, Department of Geology and Soil Science - UGCT, Krijgslaan 281, S8, 9000 Gent, Belgium, email: Hannelore.Derluyn@UGent.be; Jan.Dewanckele@UGent.be; Veerle.Cnudde@UGent.be

[4]Ghent University, Department of Physics and Astronomy - UGCT, Proeftuinstraat 86, 9000 Gent, Belgium, email: Matthieu.Boone@UGent.be

[*]Corresponding author: Hannelore Derluyn; email: Hannelore.Derluyn@UGent.be;
Ghent University, Department of Geology and Soil Science - UGCT, Krijgslaan 281, S8, 9000 Gent, Belgium

ABSTRACT

We imaged the salt solution distribution before and after crystallization and the solid crystal distribution in between repeated crystallization cycles using synchrotron X-ray microtomography. The crystallization processes of two anhydrous salts (NaCl and Na_2SO_4) and one hydrated (sodium sulfate) salt in the pore space of a natural building stone, Savonnières limestone, are studied. Synchrotron X-ray microtomography proves to be a very useful technique to study salt crystallization processes at the pore scale. The use of simultaneous phase-and-amplitude retrieval during X-ray tomographic reconstruction allows a clear segmentation of sodium sulfate solution and hydrated sodium sulfate crystals without the need for a dopant. Salt crystals can precipitate under unconfined as well as confined conditions in the multiple pore systems of Savonnières limestone, depending on their interconnection. Salt solution and salt crystals are located in mechanically weak zones of the limestone, which can be linked to damage patterns observed in this stone after repeated salt weathering cycles. The distribution and the process of pore filling by salt crystals that are revealed here advance the understanding of salt damage in porous media and may open ways to perform remediation.

KEYWORDS: limestone; salt crystallization; salt damage; segmentation; simultaneous phase-and-amplitude retrieval; synchrotron X-ray micro-computed tomography

1. INTRODUCTION

The crystallization of salts in porous building materials is one of the main causes of physical deterioration of civil engineering constructions and cultural heritage. Due to the high crystallization-induced pressures that can develop in the confined pore space, cracks may form. The risk for salt damage in building materials depends on the degree of pore filling by the crystals and the magnitude of the crystallization pressure [1]. The crystallization-induced stresses are determined by the combination of a sufficient amount of salt crystals with a sufficient high crystallization pressure. Today, there is general consensus in the literature that the crystallization pressure is a supersaturation driven phenomenon [2]-[8]. When a crystal fills a pore, a liquid film (in the order of a few nanometers [4]) remains between the crystal and the pore wall. This liquid film originates from repulsive forces between the crystal and the constraining pore wall and is necessary to allow that a crystal can grow upon its loaded surfaces. The growth upon a loaded crystal face can only exert pressure if this face is in contact with a supersaturated solution [5]. A schematic representation is given in Figure 1. The supersaturation and thus the crystallization pressure depend on the temperature and the salt solution concentration. For small pore sizes, i.e. below 0.1 μm, also the crystal curvature and the surface tension contribute to the crystallization pressure [6]. When an equilibrium situation is reached, i.e. when the crystal has its equilibrium form, the crystallization pressure uniquely depends on the surface tension and the curvature [6]. For example, for a cigar-like crystal growing in a cylindrical pore, the crystallization pressure is inversely proportional to the pore radius. This means that larger crystallization pressures occur in smaller pores. Consequently, under equilibrium conditions, the risk for salt damage increases when crystallization occurs in decreasing pore sizes. For this specific case and under the assumption of crystals in their equilibrium state, Coussy [7] derived that crystallization should start in the larger pores and consequently propagate in the smaller ones.

The depletion of the supersaturation depends on the nucleation and the growth of the salt crystals. This determines how fast the phase transitions occur and how they are spread in the porous structure. Depending on the kinetics of crystal nucleation and growth, the equilibrium state will be reached after a certain time. During the period that the kinetics are dominant, the crystallization pressure can be much larger than the values at equilibrium, due to the fact that high supersaturations can prevail. Nucleation can potentially occur in all pore ranges. Consequently, the conclusion of Coussy [7] that crystallization occurs from large to smaller pores cannot be generalized for non-equilibrium conditions during crystal nucleation and

growth and there is not necessarily a unique relationship between the pore sizes and salt damage risks. Therefore, understanding salt damage risks in porous building materials asks for detailed experimental observations of salt crystallization at the scale of the pores. The key is to determine the tridimensional distribution of salt crystals and the pore filling in a direct manner. In this paper, we make a first step in this direction. We show that a thorough understanding of the porous structure, the location of mechanically weaker zones in which stress localization can occur, and the understanding of liquid transport and the location of crystal precipitation are necessary to assess salt damage risks in the porous natural building stone studied in this paper.

Salt crystallization in porous building materials occurs over repeated cycles of crystal growth and dissolution. These cycles are due to the cyclic nature of the environmental conditions to which the materials are exposed. To reproduce these natural cycles in the laboratory, non-destructive techniques are needed to investigate the material between cycles. The study of hydrated crystals requires by definition that water needs to be kept in the sample. Thus, measurements cannot be performed by techniques such as scanning electron microscopy or mercury intrusion porosimetry. X-ray micro-computed tomography (μCT) is known to be a well suited technique to visualize and characterize the pore space of porous materials and its variations non-destructively. As the attenuation of X-rays by solutions or hydrated phases is low, other researchers enhanced the image contrast by using specific solutions such as calcium iodide solution [9]-[10], 3-bromopropyltrimethoxysilane doped water repellent or consolidant [11] or high-attenuating particles, e.g. zirconium dioxide particles [12]. Recent advances such as phase-and-amplitude retrieval [13] provide however new possibilities to image low-X-ray absorbing components such as water and hydrated salts. In this paper, we explore the possibilities offered by synchroton X-ray μCT to study the formation of anhydrous (NaCl and Na_2SO_4) and hydrated (sodium sulfate) crystals in a porous limestone, Savonnières limestone. This is done without adding a dopant, thus without possibly altering the crystallization kinetics or crystal morphology.

In the next section, we describe the studied materials, i.e. Savonnières limestone, sodium sulfate and sodium chloride salt, the experimental setup and procedure and the applied image processing and analysis techniques. In the third section, the results are described and discussed with respect to salt solution and crystal distribution and presented in comparison

with damage patterns observed in Savonnières limestone. The conclusions and possible follow-up research are formulated in the last section.

2. MATERIALS AND METHODS

2.1. Materials

2.1.1. Savonnières limestone

Savonnières limestone is a French layered oolitic limestone (Late Jurassic, Tithonian). The stone belongs to the Oolithe Vacuolaire, a stratigraphical unit (Tithonian) that also includes the Brauvillier stone, Chévillon stone, Combles stone and other local variations. Their microfacies are very diverse and are mainly characterized by hollow ooids, shell fragments, pellets and the presence of dolomite [14]-[15]. Savonnières limestone has been frequently used as a natural building stone in Belgium and the Netherlands [16] and recently for restoration purposes [17]. It is an almost pure calcitic stone (99.8% $CaCO_3$ [18]). A thin section representing the porous structure is given in the inset of Figure 2. The stone consists of spherical grains, ooids, which were formed during the deposition stage. They are developed around a nucleus and have a radial and concentric structure. Some ooids are intact, but most of them are only partly preserved. The inner structure has been dissolved during diagenesis, creating a cavity. These cavities can include only the center of the ooid or they can cover the entire ooid, leaving only the perimeter intact. They form the secondary moldic porosity. Occasionally, bivalve fragments are found. Such fragments originate from the deposition of bipartite shell moulds and are mostly hollow with a thin cortex. During deposition, layers of calcite material build up on top of each other, resulting in a preferential layering, called bedding. The ooids and shell moulds are bound by sparry calcite crystals, radially oriented on the aggregates. The sparitic calcite cement fills partly the intergranular space, resulting in triangular shaped pores. This cement is formed during diagenesis, where dissolved calcite is transported and can precipitate as sparitic calcite cement.

Four types of porosity can be distinguished in Savonnières limestone [19]: (1) the intragranular microporosity of the walls of the ooids (with two mean pore sizes of 0.1 and 0.7 μm), (2) the intergranular microporosity in between the sparitic calcite crystals (mean pore size of 12 μm), (3) the intergranular macroporosity consisting of the triangular shaped macropores in between the sparitic cement (mean pore size of 87 μm) and (4) the intragranular macroporosity or moldic porosity (also with mean pore size of 87 μm), obtained after dissolution of the ooids' calcite. The total open porosity of Savonnières limestone can

range between 22 to 41% [20]. The intergranular and intragranular macropores are only connected via smaller micropores. The macropores are forming the chambers of ink-bottle pores, while the micropores are the throats to the chambers. The macropores can thus be considered as isolated regions that are only accessible via the smaller pores. Roels et al. [19] used the wetting/drying hysteresis as a result of the presence of these ink-bottle pores to determine the pore volume distribution, presented in Figure 2.

The thin sections in Figure 3 show that the ooids can be partly detached from the surrounding calcite matrix (Figure 3a), and that microcracks can be present (Figure 3b). This type of damage can be explained by the presence of soft cores coupled with partial dissolution of cortical layers, which led to compactional crushing of ooids and shell fragments. This results in a high secondary fracture porosity. Most likely meteoric leaching of parts of the ooids weakened the ooids and allowed collapse of such grains during overburden loading [21]. Dissolution of thin interlayers within the ooid may have aided the brittle deformation, but substantial overburden stress was also required [21]. The compactional crushing induces mechanically weak zones in the Savonnières structure, creating potentially susceptible zones to salt damage.

2.1.2. Sodium sulfate and sodium chloride

Sodium sulfate and sodium chloride are two of the most damaging salts mentioned in the literature to cause building and landscape weathering (e.g. [22]-[23]). The solubility diagrams of both salts, given in Figure 4 and Figure 5, show the solubility lines, expressing the equilibrium concentration under atmospheric pressure in function of temperature for the specific salt crystal phase, when water is the solvent.

Sodium sulfate can crystallize as different phases. Under normal atmospheric conditions, the two stable phases are the decahydrate, also called mirabilite ($Na_2SO_4 \cdot 10H_2O$), and the anhydrous phase thenardite, (Na_2SO_4(V)). By cooling a sodium sulfate solution it is however often observed that mirabilite does not form directly, but that the metastable heptahydrate ($Na_2SO_4 \cdot 7H_2O$) precipitates first (e.g. [24], [25]). Upon evaporation drying of a sodium sulfate solution, the metastable Na_2SO_4(III) is frequently observed together with the stable Na_2SO_4(V) [26]. Figure 4 indicates that the solubility of the hydrated sodium sulfate crystal phases differs significantly with changing temperature. $Na_2SO_4 \cdot 10H_2O$ typically shows a

needle-like structure, whereas $Na_2SO_4 \cdot 7H_2O$ has a pyramidal shape, as depicted in Figure 4. Na_2SO_4(V) shows a prismatic structure, whereas Na_2SO_4(III) forms needle-like branches.

The solubility diagram of sodium chloride, Figure 5, shows that there is only one stable crystal phase above 0°C: halite (NaCl). Halite precipitates as cubic crystals. The solubility of sodium chloride is only slightly temperature dependent.

2.2. Sample preparation and experimental setup

Four cylindrical Savonnières samples of 3.3 mm diameter and around 5 mm height were cut to be investigated by synchrotron radiation X-ray micro-tomographic microscopy. The diameter of 3.3 mm was chosen in order to obtain samples representative for the different pore systems of the limestone. The samples were prepared to study:

1. liquid distribution in the Savonnières pore system after wetting by capillary uptake with a 2.8 molal sodium sulfate solution, with sample Ws (Wetting sulfate),
2. pore filling by salt crystals after drying of a Savonnières sample that was wet by capillary uptake with a 2.8 molal sodium sulfate solution, with sample Ds (Drying sulfate),
3. pore filling by salt crystals after drying of a Savonnières sample that was wet by capillary uptake with a 5.8 molal sodium chloride solution, with sample Dc (Drying chloride),
4. pore filling by salt solution and salt crystals after cooling of a Savonnières sample that was wet by capillary uptake with a 2.8 molal sodium sulfate solution, with sample Cs (Cooling sulfate).

The experimental setup consisted of a test chamber that can be connected to a cryojet. The chamber has an aluminum enclosure with interior dimensions of approximately 39 x 25 x 40 mm^3 and is screwed on a bridge that is overspanning the rotational stage. At the bottom side of the bridge, a silicon membrane closes the gap without hindering the stage movement. The two windows of the chamber are made out of polyimide (Kapton) foil, which is quasi transparent for X-rays. The top part, made out of plexiglass, is removable to allow placement of the sample. This part has two holes to let through the wires linking a thermocouple and a RH/temperature sensor to a data acquisition system. A custom made tube allows for connecting the test chamber with the cryojet.

The samples were glued on the sample holder with a temperature resistant silicone (GYSO-Construsil 703). Before gluing the samples Ws and Cs, they were taped circumferentially with

polyimide tape, which, in addition to transmitting X-rays well, is water and vapor tight. An X-ray tomographic dataset of the initial sample state, i.e. the reference state, was acquired for the four samples before wetting. The capillary uptake was done outside the test chamber, by bringing the upper side of the sample in contact with the salt solution for 5 minutes. The climate outside the test chamber was constant at 25°C and 30% RH. The 2.8 molal sodium sulfate solution was put on a hot plate at 40°C, ensuring undersaturation of the solution with respect to the different crystal phases. This state is indicated on the solubility diagram, given in Figure 4, by the black point.

After wetting the samples Ws and Cs, the top side was closed with a vapor tight mastic paste in order to acquire tomographic datasets without loss of moisture. The cryojet was set up to provide a flow of cold air at -6°C for sample Cs inside the test chamber. The cooling induces the nucleation and growth of hydrated sodium sulfate crystals. The metastable heptahydrate is expected to form in sample Cs (Figure 4, short dashed line).

For the samples Ds and Dc, repeated wetting-drying cycles were performed in order to accumulate salt crystals. The cryojet produced a flow of warm air at 80°C; this temperature induces a fast receding drying front and thus precipitation of the salt crystals inside the sample. A tomographic dataset was acquired of the dry state of every cycle. Following the phase diagram of sodium sulfate, Na_2SO_4 is expected to form in sample Ds (Figure 4, dashed line). In sample Dc, NaCl forms (Figure 5, dashed line).

2.3. Synchrotron radiation X-ray microtomography

Synchrotron radiation X-ray tomographic microscopy was performed at the TOMCAT beamline of the synchrotron radiation facility Swiss Light Source of the Paul Scherrer Institute, Villigen, Switzerland [27]. The TOMCAT beamline gets photons from a 2.9 T magnetic dipole, corresponding to a critical energy of 11.1 keV, generating a closely bundled and highly brilliant X-ray beam. A fixed-exit double crystal multilayer monochromator (DCMM) is used to select X-rays with a photon energy bandwidth of a few percent. In our experiment, the DCMM was set up to obtain a central X-ray photon energy of 32 keV. The TOMCAT X-ray detector was put at a distance of approximately 1 cm from the test chamber, to prevent damaging the detector while cooling or heating of the chamber enclosure. The resulting sample-detector distance was around 25 mm. The X-ray detector consisted of a 20 µm thick LAG scintillator able to convert the X-rays into visible light. The light then passes

through an optical microscope, gets reflected in a mirror and is finally captured on a 2048 x 2048 pixels CCD camera with a 14 bit dynamic range. The microscope configuration, with a 4x objective, led to a maximum field of view of approximately 3.8 x 3.8 mm^2. Each radiographic image was binned at the hardware level (CCD camera) by a factor 2 x 2. The field of view was cropped in order to only focus on the interesting region of our samples. This resulted in radiographic images of 1024 x 664 pixels. The voxel size with this setup is 3.7 µm. Recalling the pore volume distribution of Savonnières limestone, as shown in Figure 2, this means that we can observe the macropores of Savonnières limestone, and we can partly observe the intergranular micropores in between the sparitic calcite crystals. We can however not distinguish the microporosity of the ooid walls from the calcite matrix. The intergranular micropores and the micropores of the ooid walls, which cannot be resolved, are the accessibility pores for the macropores.

For each tomographic dataset, 1441 radiographic projections were made at equiangular positions over a total rotation angle of 180 degrees. The exposure time for each radiographic measurement was of the order of 320 milliseconds. 144 flat-field and 32 dark-field images were acquired before the start of each tomographic scan and 144 flat-field images after the scan, in order to compensate for the non-uniformity of the beam and the detector and the presence of noisy pixels in the CCD detector. The total scanning time was around 10 minutes.

2.4. Image processing and analysis

After the correction of the radiographs for hot pixels and ring artifacts, the tomographic datasets are reconstructed in a standard way based on the X-ray absorption of the sample using a filtered backprojection (FBP) algorithm for parallel projection data [28] in the software Octopus from inCT, Belgium [29]. Here, the amplitude and the phase of the X-ray waves are considered together (mixed amplitude-and-phase images). No beam hardening correction is needed due to the small bandwidth of the X-ray beam.

The aim of samples Ds and Dc is to examine the distribution of anhydrous sodium sulfate and sodium chloride crystals in Savonnières limestone. As the attenuation coefficients of $CaCO_3$ (limestone), Na_2SO_4 and NaCl are in the same range, it is only possible to distinguish the salt crystals from the stone matrix in samples Ds and Dc by subtracting the reference dataset of the initial sample state from the dataset containing crystals. The sample stage at the TOMCAT beamline ensures that the sample holder is placed at the same position. Only small shifts (a

few voxels) between repeated scans of the same sample are observed. These shifts are corrected by aligning the datasets using the Align3TP plugin [30] in the software ImageJ [31] before subtraction. After subtraction, the volume of salt crystals remains.

The aim of samples Ws and Cs is to study the distribution of salt solution and of hydrated sodium sulfate crystals in Savonnières limestone. For these samples, it is not possible to segment the liquid phase and the hydrated sodium sulfate crystal phase by subtracting the reference dataset of the sample after the standard reconstruction (FBP) as the difference in gray values between the air phase and the salt solution or the hydrated crystals is too small. Thresholding based on the image histogram is therefore also not possible. As can be seen on the histogram of sample Ws in Figure 6, the air and liquid containing phases are lumped together in one peak. To solve this problem, a second reconstruction is done, consisting of an extra processing step on the normalized images before employing the backprojection algorithm for the tomographic reconstruction. The extra step consists of simultaneous phase-and-amplitude retrieval (SPAR) [13], [32]. Both the absorption and the phase shift of the X-rays are now considered separately and are assumed to be proportional in a homogeneous object. This algorithm retrieves the sample thickness from the mixed phase-and-amplitude images, thus reducing the phase artifacts. Additionally, the signal-to-noise ratio is improved by using this method [33]. The use of SPAR results in image histograms showing a clear distinction between the different components, as shown in Figure 6. The air and liquid phase are now in a different range of gray values, making it possible to threshold the liquid phase directly from the image histogram.

The pore space was further analyzed with the software Morpho+ [34]. The datasets were first filtered to improve the signal-to-noise ratio, using the bilateral filter. The volume-of-interest (VOI) of samples Ds and Dc was defined using the dataset of the samples at the reference state, so that the boundary of the VOI coincides with the outer surface of the sample. The VOI of samples Ws and Cs was defined as a cylinder with radius 3.3 mm, so that the polyimide foil was excluded. The ‘artificial pore space’ created between the foil and the sample’s surface was included in the VOI, as the salt solution also filled this space and salt crystals precipitated there. We characterized the porosity and the connectivity of the samples’ pore structure. As the samples are small, the majority of the pores are characterized as pores in direct contact with the outer surface, or connected to the surface via throats resolvable within the spatial resolution of 3.7 μm. The remaining pores are connected via throats of a size below

the spatial resolution and are not visible in the images.

The obtained volumes of stone matrix, liquid phase and salt crystal phase, and of the pore space, are visualized with VGStudio MAX 2.1 from Volume Graphics. Further on, the stone matrix is colored in light gray, the liquid phase in blue and the salt crystals in red. The pores that are directly connected to the surface or that are connected via throats resolvable within the spatial resolution are colored in dark gray. The pores connected via throats below the spatial resolution are represented in green. The results obtained from the image analysis are described and discussed in the next section.

3. RESULTS AND DISCUSSION

3.1. Salt solution distribution after capillary uptake

A horizontal cross section of the sample Ws in its wet state is shown in Figure 7. This sample has a total porosity of 16%, while 56% of the porosity is occupied by the salt solution after initial wetting. A close-up of its top part is given in Figure 8. Figure 8a represents the stone structure without solution, showing that the calcite grains in the intergranular pores are clearly resolved with the X-ray μCT technique. Figure 8b represents the distribution of the solution after the capillary uptake and shows that the larger intergranular and the intragranular macropores do not get filled. Liquid clusters are observed in between the calcite grains, forming a liquid film on the surface of the pores in which surface flow can occur. This can be also seen in the close-up A of Figure 7. This inset additionally shows that corners of the intergranular macropores get filled, by which transport can occur through corner flow. The capillary meniscus can be clearly observed. These observations are similar to the ones made by Roels et al. [35] with SEM-visualization of Savonnières samples exposed to capillary uptake of an epoxy resin.

From Figure 7 we furthermore observe that the majority of the micropores, as detected given the resolution, and the smaller pores of the intergranular macroporosity are filled with salt solution. The weak mechanical zones corresponding to the secondary porosity resulting from compaction get (partly) filled by salt solution. Inset B shows the filling of a microcrack through an ooid. Inset C and D show that the pore space created by the detachment of the ooids, i.e. the elongated pores formed where the contact between the ooid and the calcite matrix is broken, is also penetrated by salt solution. When these pores are not completely filled, the capillary meniscus is observed. In addition, inset C and D show that liquid films

form in the hollows of the ooids as well, i.e. in the secondary moldic porosity.

The observed imbibition process is related to the capillary action in the coupled pore system of Savonnières limestone. The intragranular micropores, which cannot be resolved in the tomography images, and the intergranular micropores, which are partly resolved, are the accessibility pores, i.e. the throats of the ink-bottle pores. They connect the inter- and intragranular macropores, i.e. the chambers of the ink-bottle pores, to the environment. In a simplified way, we could picture Savonnières limestone as a porous structure of coarse porous inclusions embedded in a fine pore network. The fine pore network plays the main role during capillary uptake. It sucks the solution into the structure and supplies it to the coarse porous inclusions. Due to air entrapment and the lower capillary suction in the coarse pores, the inclusions do not get filled [35], only liquid films form on the surface and in the corners. The saturation of the inclusions would require a much longer contact time with the salt solution than we used in our experiments, in order for the entrapped air to dissolve. Or it would require an experiment at a higher intrusion pressure [36], e.g. a vacuum saturation test or a mercury intrusion test. The micropores also supply solution to the secondary fracture porosity, i.e. the porosity created by microcracks and delamination of the ooids, which fills itself by capillary suction.

3.2. Salt crystal distribution after drying

Samples Ds and Dc are subjected to repeated wetting-drying cycles. As mentioned above, drying is induced fast by imposing a temperature of 80°C in the test set-up. By doing so, salt crystals precipitate both inside the sample and on the surface of the sample. Figure 9 shows horizontal cross sections of sample Dc after the first, the second and the third wetting-drying cycle with a 5.8 molal sodium chloride solution. A close-up of the three areas marked by the white rectangles is given on the right side. We observe that salt crystals grow on the pore wall of the macropores, i.e. in the secondary moldic porosity, and in the intergranular macropores, they form in the elongated pore spaces, i.e. the secondary porosity originating from the delamination of the ooids, and they form in microcracks that are present in the stone matrix. The locations of the salt crystals correspond to locations where the salt solution penetrated as described in section 3.1.

The close-up images in Figure 9 clearly illustrate the accumulation of salt crystals with every cycle. The initial total porosity of the sample is 17.1%. After the first wetting-drying cycle,

391 the total porosity decreases to 15%, due to the presence of solid salt crystals. In the second
392 and third cycle, the total porosity decreases to 11.6% and 10.8%, respectively. The
393 accumulation is caused by the continuous increase of salt ions in the pore space with every
394 wetting cycle. We can assume that the loss of ions due to dissolution and transport towards
395 the surface during the rewetting phases was limited, as the salt solution was highly
396 concentrated and only a short wetting time of about 5 minutes was imposed, immediately
397 followed by drying.
398
399 Two main crystallization phenomena are observed. In the macropores, e.g in the hollow ooid
400 magnified in Figure 9, a salt crust builds up. This crust grows from the liquid film present on
401 the pore wall. Once the crust has formed, it can act itself as a porous medium [37] building up
402 additional layers of salt crystals. In this process, the micropores surrounding the macropores
403 supply the salt solution to form the liquid film or to penetrate the salt crust. As this salt crust
404 grows freely in the macropore, we can consider this crystallization as a harmless efflorescence
405 within the porous structure. These crystals grow under unconfined conditions, meaning that
406 they are not enclosed by the pore wall. In the microcracks and pores originating from
407 delamination of the ooids and in the small pores of the intergranular macroporosity, salt
408 crystals fill up the pore space, i.e. they grow under confined conditions. In these locations,
409 potentially high crystallization pressures can develop and induce crystallization damage.
410 Therefore, we can conclude that salt crystals can precipitate under unconfined as well as
411 confined conditions in multiple pore systems depending on their interconnection. Within the
412 obtained spatial resolution, we find harmless crystallization in the large macropores (hundreds
413 of µm range) and potentially harmful crystallization in the mechanically weaker zones created
414 by the secondary fracture porosity (tenths of µm range). The same observations were made
415 for the sample Ds, for which a close-up of the first and the fourth cycle is given in Figure 10.
416 Two hollow ooids are indicated by the white arrows in Figure 10a. Inside these ooids, a salt
417 crust of Na_2SO_4 grows. Two delaminated ooids are circled in Figure 10a. The amount of
418 crystals increases in their secondary fracture porosity.
419
420 **3.3. Salt crystal distribution after cooling**
421 Sample Cs is capillary saturated with a 2.8 molal sodium sulfate solution at 40°C and
422 consecutively cooled to a temperature of -6°C in the experimental setup. A vertical cross
423 section of the sample is given in Figure 11. The image shows the state of the sample after 10
424 minutes of cooling. The total porosity amounts to 24.9%. The hydrated salt crystals occupy

31.1% of the total porosity, the remaining salt solution occupies 15.8%. The other 53.1% of the porosity is filled by air. We observe that large hydrated crystals form in the macropores; a close-up of one macropore is given in Figure 12. The crystal shape in Figure 12 has a (bi)pyramidal structure, which is the shape reported for heptahydrate crystals. The crystallization in the macropore magnified in Figure 11 (inset A) resembles only partly the typical representation of crystallization in a cylindrical pore, as illustrated in the inset. The liquid, the crystal and the gas phase coexist in the pore space. The crystal shape is however more comlex than given by the schematic representation. The shape is determined by the crystal phase and by the structure of the pore system in which it precipitates. In the macropores that got filled by salt solution, the crystal is enclosed by the pore wall. Thus the crystal is exposed to confined conditions and crystallization pressures can develop. Also in the secondary fracture porosity, confined crystallization takes place. Inset B shows that inside ooids with a microporous structure in their center, small crystals form in coexistence with the liquid and the gas phase. As for the drying experiments, crystallization occurs in different pore systems, i.e. in large and smaller pores, of the Savonnières limestone. The crystallization is thus far more complex than what can be understood from a cylindrical capillary tube model. We remark that our observations are particular for a small sample. In a large stone piece, the macropores will be less filled, as they form the chambers of ink-bottle pores. Due to the need for a small sample size and the application of the polyimide tape on sample Cs, creating artificial pore space, more macropores got filled by the salt solution.

3.4. Discussion

The results suggest that salt crystals precipitate in all the pore systems of Savonnières limestone. Crystals can partly fill the macropores as they can grow from the liquid film present on the pore wall of the macropores. Crystals are also observed in the microporous structure of the center of intact ooids. Furthermore, crystals form in microcracks and in pores resulting from the delamination of ooids, or they can fill up small intergranular macropores.

The most important observation, with respect to salt crystallization damage, is that both salt solution and salt crystals are present in mechanically weak zones of the stone, where there is less cohesion between the ooids and the calcite matrix (Figure 3a) or between the calcite grains. In the initial material matrix, weaknesses can already be present as microcracks crossing the ooids and the calcite grains, as illustrated in Figure 3b. The weak zones originate from the secondary fracture porosity. One can imagine that when crystallization pressures act

in these pores, the pore walls are pushed apart and these 'fracture pores' open further, by which macroscopic fracturing can propagate in the structure. Therefore we deduce that cracks can form in Savonnières limestone due to confined in-pore salt crystallization. Figure 13a and Figure 13b show the crack pattern in the upper part of Savonnières limestone samples subjected to repeated wetting drying cycles with a 1.4 molal sodium sulfate solution and a 5.8 molal sodium chloride solution, respectively. The samples are square prisms of 10 x 10 mm^2 base and 15.5-16 mm height, hydrophobically treated on their upper part, in order that salt crystals would accumulate in a limited zone. The average penetration depth of the treatment was around 3.5 mm. The samples were sealed on their lateral sides so that one dimensional wetting and drying occurred. They were visualized by laboratory X-ray micro-CT as described by Derluyn et al. [38]. More details on the wetting-drying induced salt damage in these samples can be found in [38] and [39]. The cracks form around ooids and through ooids, examples are indicated by the white arrows in Figure 13a and Figure 13b. Hence the crack pattern follows weaknesses, i.e. pre-existing flaws, in the stone matrix, corresponding to the locations of salt solution paths during capillary uptake and of crystallization described in this paper. This crack pattern has also been described by Fronteau [18] after the study of damage cases in the field in Savonnières limestone.

4. CONCLUSIONS

We imaged salt solution distribution before and after crystallization and crystal distribution in between repeated crystallization cycles of two anhydrous salts (NaCl and Na_2SO_4) and one hydrated (sodium sulfate) salt in the pore space of Savonnières limestone. Images clearly indicate that salt solution and salt crystals are located in mechanically weak zones of Savonnières limestone, which can be linked to damage patterns observed in this stone during salt weathering cycles. Interpreting the distribution and the process of pore filling by salt solution and salt crystals can advance the understanding of salt damage in porous media and may open ways to perform remediation. In effect, the presence of salt crystals in mechanically weaker zones gives an indication of the susceptibility of the porous material to crystallization damage. In the case of the Savonnières stone, remediation techniques could focus on promoting harmless efflorescence inside the macropores and preventing crystal growth in the mechanically weak zones of the secondary fracture porosity. This can possibly be done by, for example, the use of crystallization inhibitors [40]-[41].

Furthermore, the results presented in this paper show that synchrotron X-ray μCT is a

valuable tool to examine crystallization processes occurring in the pore space of porous building materials. It allows locating the distribution of salt solutions and of salt crystals in the pore space, and assessing if the location coincides with mechanically weaker zones, i.e. pre-existing flaws, in the original material structure. The pore filling by salt solution and salt crystals can be evaluated in a non-destructive way, which allows studying repeated crystallization cycles and the distribution of solutions and hydrated crystals. We have shown that using simultaneous phase-and-amplitude-retrieval during reconstruction of a monomineralic limestone allows for a clear segmentation of salt solution, hydrated salt crystals and air in its pore space. No contrast enhancement by the use of a specific salt or a dopant is needed, by which the crystallization kinetics remain unaltered. This technique could be useful in the future to study freezing processes inside porous structures in 3D. In order to visualize a representative volume of the pore space, the voxel size of our study is 3.7 μm. As a consequence, we could not observe the processes taking place in the microporosity of the stone. Future work could focus only on a part of the representative volume, using local tomography or 3D X-ray nano imaging [42], by which the spatial resolution can be increased and smaller pores to a resolution below 200 nm become visible.

5. ACKNOWLEDGEMENTS

This work is based on experiments performed at the TOMCAT beamline at the Swiss Light Source, Paul Scherrer Institute, Villigen, Switzerland. The preliminary discussions with Julie Fife, the technical help of Gordan Mikuljan and the assistance of Michele Griffa, Tim De Kock, Sevi Modestou and Peter Modregger during the beamtime are greatly appreciated. IWT-Flanders is acknowledged for its grant to Jan Dewanckele.

6. REFERENCES

[1] H. Derluyn, P. Moonen, J. Carmeliet, Deformation and damage due to drying-induced salt crystallization in porous limestone, J. Mech. Phys. Solids (2013) accepted.

[2] G.W. Scherer, Crystallization in pores, Cement Concrete Comp. 29 (1999) 1347–1358.

[3] R.J. Flatt, Salt damage in porous materials: how high supersaturations are generated, J. Cryst. Growth 242 (2002) 435–454.

[4] G.W. Scherer, Stress from crystallization of salt, Cement Concrete Res. 34 (2004) 1613–1624.

[5] M. Steiger, Crystal growth in porous materials - I: The crystallization pressure of large crystals, J. Cryst. Growth 282 (2005) 455–469.

[6] M. Steiger, Crystal growth in porous materials - II: Influence of crystal size on the crystallization pressure, J. Cryst. Growth 282 (2005) 470–481.

[7] O. Coussy, Deformation and stress from in-pore drying-induced crystallization of salt, J. Mech. Phys. Solids 54 (2006) 1517–1547.

[8] R.J. Flatt, M. Steiger, G.W. Scherer, A commented translation of the paper by C.W. Correns and W. Steinborn on crystallization pressure, Environ. Geol. 52 (2007) 187–203.

[9] N. Shokri, P. Lehmann, D. Or, Liquid-phase continuity and solute concentration dynamics during evaporation from porous media: Pore-scale processes near vaporization surface, Phys. Rev. E 81 (2010) 046308.

[10] N. Shokri, M. Sahimi, Structure of drying fronts in three-dimensional porous media, Phys. Rev. E 85 (2012) 066312.

[11] V. Cnudde, J.P. Cnudde, C. Dupuis, P.J.S. Jacobs, X-ray micro-CT used for the localization of water repellents and consolidants inside natural building stones, Mater. Charact. 53 (2004) 259–271.

[12] J.-F. Gaillard, C. Chen, S.H. Stonedahl, B.L.T. Lau, D.T. Keane, A.I. Packman, Imaging of colloidal deposits in granular porous media by X-ray difference micro-tomography, Geophys. Res. Lett. 34 (2007) 2–6.

[13] M.N. Boone, W. Devulder, M. Dierick, L. Brabant, E. Pauwels, L. Van Hoorebeke, Comparison of two single-image phase-retrieval algorithms for in-line x-ray phase-contrast imaging, J. Opt. Soc. Am. A 29 (2012) 2667–2672.

[14] G. Fronteau, C. Schneider-Thomachot, E. Chopin, V. Barbin, D. Mouze, A. Pascal, Black-crust growth and interaction with underlying limestone microfacies, Geological Society, London, Special Publications, 333 (2010) 25-34.

[15] N. Schiavon, BSEM study of decay mechanisms in urban oolitic limestones, Eur. Cult. Herit. 6 (1992) 35-46.

[16] R.P.J. van Hees, H. De Clercq, W.J. Quist, Stenen van binnen, stenen van buiten. Natuursteen in de jonge bouwkunst. Syllabus 4de Vlaams-Nederlandse Natuursteendag., Delft/Rotterdam, 2012.

[17] R. Dreesen, M. Dusar, Historical building stones in the province of Limburg (NE Belgium): role of petrography in provenance and durability assessment, Mater. Charact. 53 (2004) 273–287.

559 [18] G. Fronteau, Comportements telogénétiques des principaux calcaires de Champagne-
560 Ardenne, en relation avec leur facies de dépôt et leur séquençage diagénétique,
561 Université de Reims Champagne-Ardenne, France, 2000.
562 [19] S. Roels, J. Elsen, J. Carmeliet, H. Hens, Characterisation of pore structure by
563 combining mercury porosimetry and micrography, Mater. Struct. 34 (2001) 76–82.
564 [20] CATED, Les pierres de France: pierres calcaires - roches marbrières - granit - grès,
565 Editions du Moniteur, Paris, 1980.
566 [21] P.A. Scholle, D.S. Ulmer-Scholle, A color guide to the petrography of carbonate rocks,
567 American Association of Petroleum Geologists, Tulsa, USA, 2003.
568 [22] J.P. McGreevy, B.J. Smith, Salt weathering in hot deserts: observations on the design
569 of simulation experiments, Geogr. Ann. A 64 (1982) 161–170.
570 [23] A. Goudie, H. Viles, Salt Weathering Hazards, Wiley, Chichester, 1997.
571 [24] L. Rijniers, H. Huinink, L. Pel, K. Kopinga, Experimental evidence of crystallization
572 pressure inside porous media, Phys. Rev. Lett. 94 (2005) 23–26.
573 [25] H. Derluyn, T.A. Saidov, R.M. Espinosa-Marzal, L. Pel, G.W. Scherer, Sodium sulfate
574 heptahydrate I: The growth of single crystals, J. Cryst. Growth 329 (2011) 44–51.
575 [26] K. Linnow, A. Zeunert, M. Steiger, Investigation of sodium sulfate phase transitions in
576 a porous material using humidity- and temperature-controlled X-ray diffraction., Anal.
577 Chem. 78 (2006) 4683–4689.
578 [27] M. Stampanoni, A. Groso, A. Isenegger, G. Mikuljan, Q. Chen, D. Meister, et al.,
579 TOMCAT: A beamline for TOmographic Microscopy and Coherent rAdiology
580 experimenTs, AIP Conf. Proc. 879 (2007) 848–851.
581 [28] A.C. Kak, M. Slaney, Principles of Computerized Tomographic Imaging, IEEE Press,
582 New York, 1988.
583 [29] J. Vlassenbroeck, M. Dierick, B. Masschaele, V. Cnudde, L. Van Hoorebeke, P.
584 Jacobs, Software tools for quantification of X-ray microtomography at the UGCT,
585 Nucl. Instrum. Meth. A 580 (2007) 442–445.
586 [30] J.A. Parker, Align3 TP Manual, 2004.
587 [31] C.A. Schneider, W.S. Rasband, K.W. Eliceiri, NIH Image to ImageJ: 25 years of image
588 analysis, Nature Methods 9 (2012) 671–675.
589 [32] D. Paganin, S.C. Mayo, T.E. Gureyev, P.R. Miller, S.W. Wilkins, Simultaneous phase
590 and amplitude extraction from a single defocused image of a homogeneous object., J.
591 Microsc. 206 (2002) 33–40.

[33] M.N. Boone, Y. De Witte, M. Dierick, A. Almeida, L. Van Hoorebeke, Improved signal-to-noise ratio in laboratory-based phase contrast tomography., Microsc. Microanal. 18 (2012) 399–405.

[34] L. Brabant, J. Vlassenbroeck, Y. De Witte, V. Cnudde, M.N. Boone, J. Dewanckele, et al., Three-dimensional analysis of high-resolution X-ray computed tomography data with Morpho+, Microsc. Microanal. 17 (2011) 252–263.

[35] S. Roels, J. Carmeliet, H. Hens, J. Elsen, Microscopic analysis of imbibition processes in oolitic limestone, Geophys. Res. Lett. 27 (2000) 3533–3536.

[36] J. Carmeliet, S. Roels, Determination of the Moisture Capacity of Porous Building Materials, J. Build. Phys. 25 (2002) 209–237.

[37] N. Sghaier, M. Prat, Effect of efflorescence formation on drying kinetics of porous media, Transport Porous Med. 80 (2009) 441–454.

[38] H. Derluyn, M. Griffa, D. Mannes, I. Jerjen, J. Dewanckele, P. Vontobel, et al., Characterizing saline uptake and salt distributions in porous limestone with neutron radiography and X-ray micro-tomography, J. Build. Phys. 36 (2013) 353–374.

[39] H. Derluyn, Salt transport and crystallization in porous limestone: neutron - X-ray imaging and poromechanical modeling, Diss. ETH No. 20673, ETH Zurich, Switzerland, 2012.

[40] S. Gupta, K. Terheiden, L. Pel, A. Sawdy, Influence of Ferrocyanide Inhibitors on the Transport and Crystallization Processes of Sodium Chloride in Porous Building Materials, Cryst. Growth Des. 12 (2012) 3888–3898.

[41] E. Ruiz-Agudo, C. V. Putnis, L. Pel, C. Rodriguez-Navarro, Template-Assisted Crystallization of Sulfates onto Calcite: Implications for the Prevention of Salt Damage, Cryst. Growth Des. 13 (2013) 40–51.

[42] M. Holler, J. Raabe, A. Diaz, M. Guizar-Sicairos, C. Quitmann, A. Menzel, et al., An instrument for 3D x-ray nano-imaging., Review Sci. Instrum. 83 (2012) 073703.

[43] H. Hartley, B.M. Jones, G.A. Hutchinson, The spontaneous crystallization of sodium sulfate solutions J. Chem. Soc. Transactions 93 (1908) 825–833.

[44] M. Steiger, S. Asmussen, Crystallization of sodium sulfate phases in porous materials: The phase diagram Na_2SO_4-H_2O and the generation of stress Geochim. Cosmochim. Ac. 72 (2008) 4291–4306.

[45] M. Steiger, J. Kiekbusch, A. Nicolai, An improved model incorporating Pitzer's equations for calculation of thermodynamic properties of pore solutions implemented into an efficient program code Constr. Build. Mater. 22 (2008) 1841–1850.

FIGURES

Figure 1. Representation of a crystal in a cylindrical pore. A liquid film is maintained between the crystal surface and the pore wall. The crystallization pressure expresses the difference between the pressure acting on the loaded crystal face p_{cr} and the pressure acting on the unloaded crystal face p_l.

Figure 2. Pore volume distribution of Savonnières limestone, with the top inset showing a thin section of the stone. The figure represents (1a-1b) the intergranular micropores of the ooids, (2) the intergranular micropores in between the sparitic calcite crystals, (3) the intergranular macropores and (4) the intragranular macropores. The pore systems 1a and 1b cannot be resolved in the X-ray micro-computed tomography datasets as the voxel size is limited to 3.7 μm.

Figure 3. Apparently mechanically weak zones, indicated by the white arrows, in the pore structure of Savonnières limestone, visualized by a petrographic microscope: (a) detached ooid, (b) microcracks in the stone matrix.

Figure 4. Solubility diagram of sodium sulfate in the temperature range -10 – 90°C [43], [44]. The solubility lines of the different sodium sulfate crystal phases are given: heptahydrate, $Na_2SO_4 \cdot 7H_2O$ (inset A); decahydrate (mirabilite), $Na_2SO_4 \cdot 10H_2O$ (inset B); thenardite, Na_2SO_4(V) (inset C); and Na_2SO_4(III) (inset D). In addition, the heptahydrate supersolubility line and ice line are presented. The cooling process of sample Cs is indicated by the short dashed line and the drying process of sample Ds by the dashed line. The dashed lines give an indication of a possible temperature-concentration evolution, but do not necessarily represent the exact evolution in the sample.

Figure 5. Solubility diagram of sodium chloride in the temperature range 0 – 90°C [45]: halite, NaCl, anhydrous salt. The cubic crystal structure of halite is represented in the inset figure. The drying process of sample Dc is indicated by the dashed line. The dashed line gives an indication of the possible temperature-concentration evolution.

Figure 6. Histogram of sample Ws after a standard filtered backpojection (FBP) reconstruction, based on mixed projection images; and after a reconstruction based on simultaneous phase-and-amplitude retrieval (SPAR).

Figure 7. Horizontal cross section of sample Ws, with the sodium sulfate solution in blue and the not wetted porosity in dark gray and green. Close-ups of the areas marked by the white rectangles are given in the four inset figures. The scale bar in the inset figures represents 0.2 mm.

Figure 8. Close-up on the top part of Figure 7 (area A and surrounding), without coloring of the porosity. (a) The calcite grains of the oolitic structure of Savonnières limestone are clearly seen in the initial state. (b) After capillary uptake, the solution forms liquid clusters in between the grains.

Figure 9. Distribution of NaCl crystals, colored in red, in the sample Dc after (a) the first, (b) the second and (c) the third wetting-drying cycle with a 5.8 molal sodium chloride solution. The porosity is represented in dark gray and green. On the right side, a close-up of the areas indicated by the white rectangles in figure (a) is given.

Figure 10. Distribution of Na_2SO_4 crystals, colored in red, in a part of the sample Ds after (a) the first and (b) the fourth wetting-drying cycle with a 2.8 molal sodium sulfate solution. The porosity is colored in dark gray and green. In the secondary porosity of hollow oolites (indicated by the white arrows in figure a), a salt crust builds up. In the secondary porosity of detached oolites (white circled in figure a) Na_2SO_4 accumulates.

Figure 11. Distribution of hydrated sodium sulfate crystals, in red, and salt solution, in blue, after cooling sample Cs. The not wetted porosity is represented in dark gray and green. Close-ups of the areas marked by the white rectangles are given in the inset figures. Inset A partly resembles the schematic representation from the literature of a crystal in a cylindrical pore (see also Figure 1). The scale bar in the inset figures represents 0.2 mm.

Figure 12. Close-up of a macropore in sample Cs. The hydrated sodium sulfate crystals are represented in red. The liquid phase and the porosity are not visualized for clarity. The crystal shape suggests that the hydrated crystal is sodium sulfate heptahydrate.

Figure 13. Zoom on the vertical cross section of two Savonnières samples, as described by [38], (a) after 4 wetting-drying cycles with 1.4 molal Na_2SO_4-solution and (b) after 3 wetting-drying cycles with 5.8 molal NaCl-solution. The white arrows point to cracks formed around ooids and through ooids.

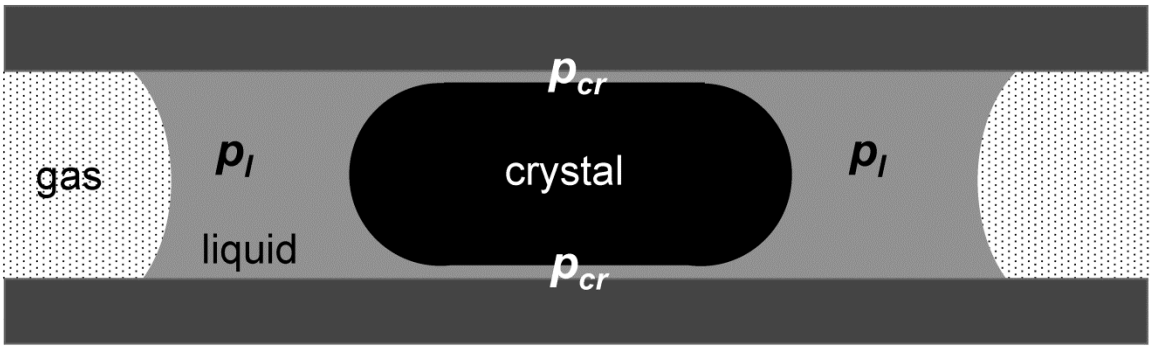

686

687 Figure 1. Representation of a crystal in a cylindrical pore. A liquid film is maintained between
688 the crystal surface and the pore wall. The crystallization pressure expresses the difference
689 between the pressure acting on the loaded crystal face p_{cr} and the pressure acting on the
690 unloaded crystal face p_l.

691

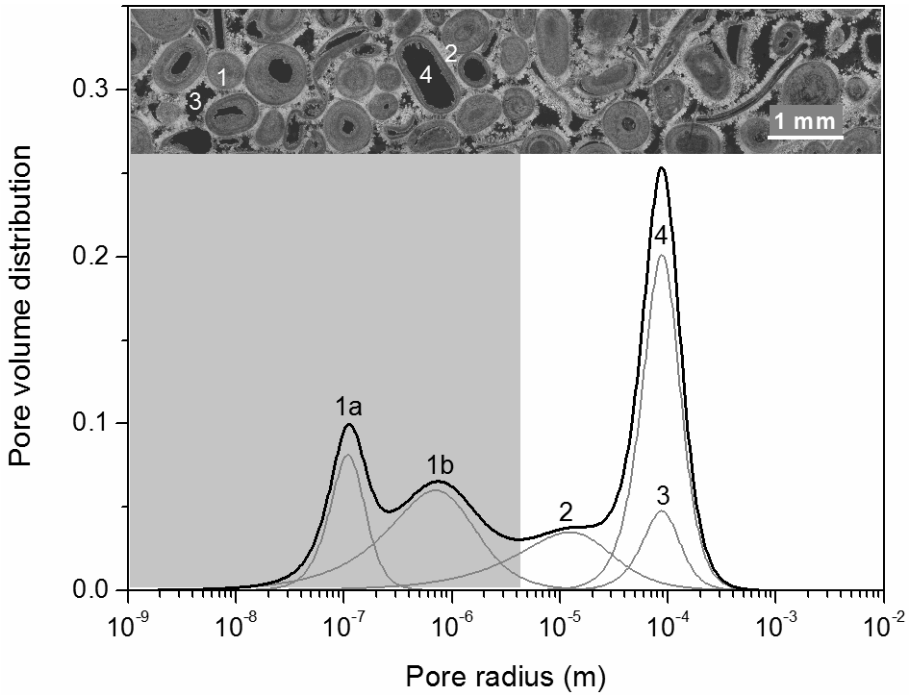

692

693 Figure 2. Pore volume distribution of Savonnières limestone, with the top inset showing a thin
694 section of the stone. The figure represents (1a-1b) the intergranular micropores of the ooids,
695 (2) the intergranular micropores in between the sparitic calcite crystals, (3) the intergranular
696 macropores and (4) the intragranular macropores. The pore systems 1a and 1b cannot be
697 resolved in the X-ray micro-computed tomography datasets as the voxel size is limited to 3.7
698 μm.

699

(a)

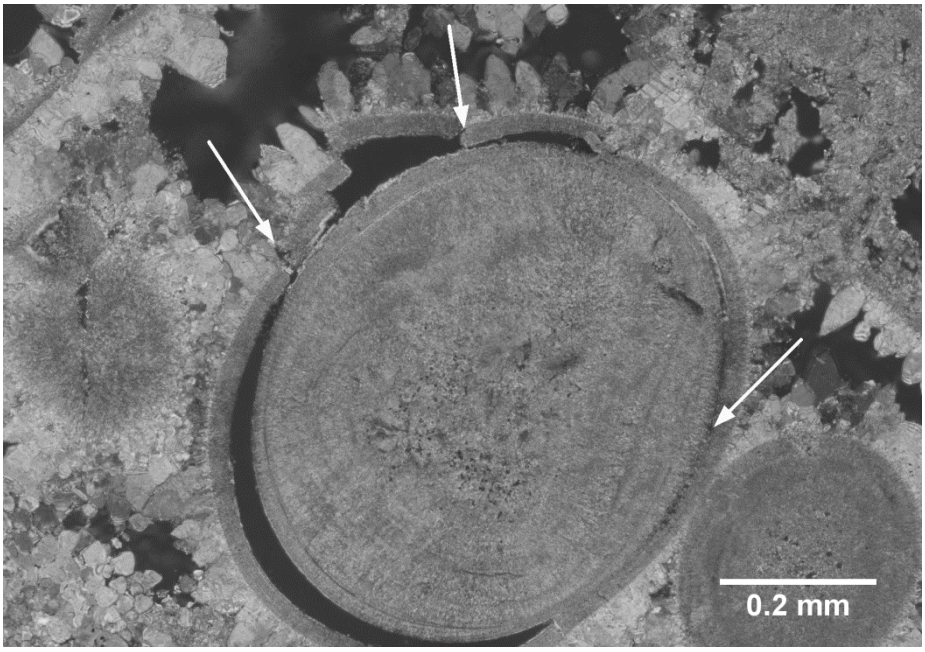

(b)

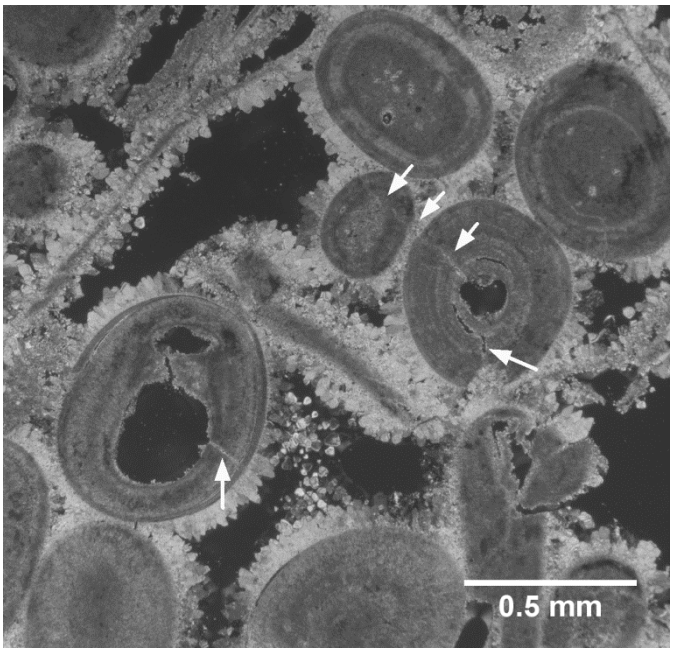

Figure 3. Apparently mechanically weak zones, indicated by the white arrows, in the pore structure of Savonnières limestone, visualized by a petrographic microscope: (a) detached ooid, (b) microcracks in the stone matrix.

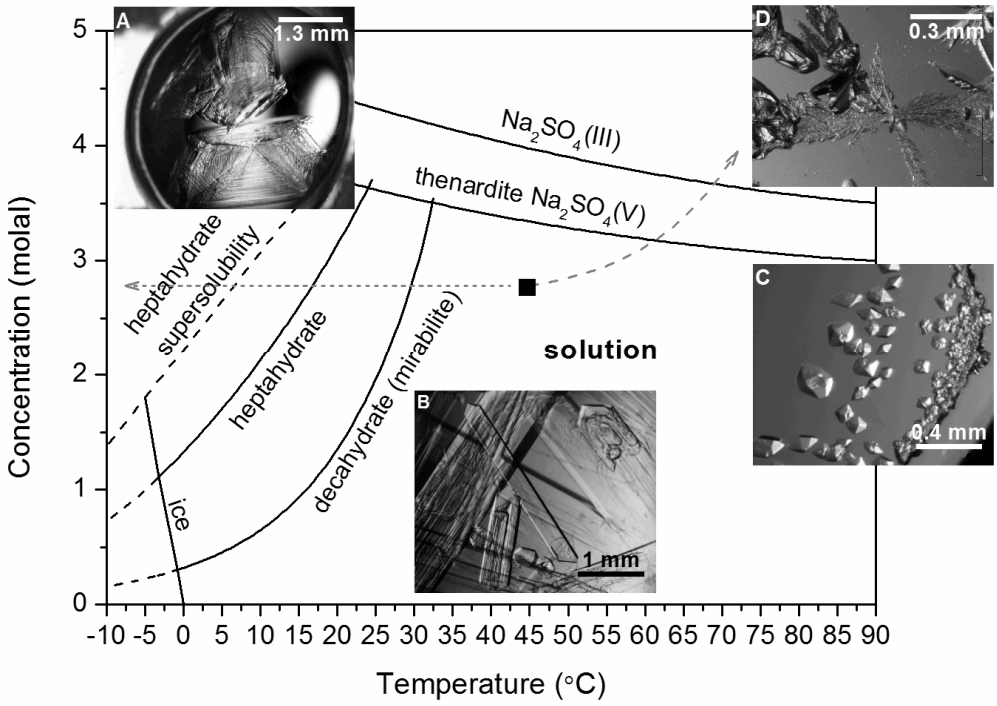

708

709

710 Figure 4. Solubility diagram of sodium sulfate in the temperature range -10 – 90°C [43], [44].
711 The solubility lines of the different sodium sulfate crystal phases are given: heptahydrate,
712 $Na_2SO_4 \cdot 7H_2O$ (inset A); decahydrate (mirabilite), $Na_2SO_4 \cdot 10H_2O$ (inset B); thenardite,
713 Na_2SO_4(V) (inset C); and Na_2SO_4(III) (inset D). In addition, the heptahydrate supersolubility
714 line and ice line are presented. The cooling process of sample Cs is indicated by the short
715 dashed line and the drying process of sample Ds by the dashed line. The dashed lines give an
716 indication of a possible temperature-concentration evolution, but do not necessarily represent
717 the exact evolution in the sample.

718

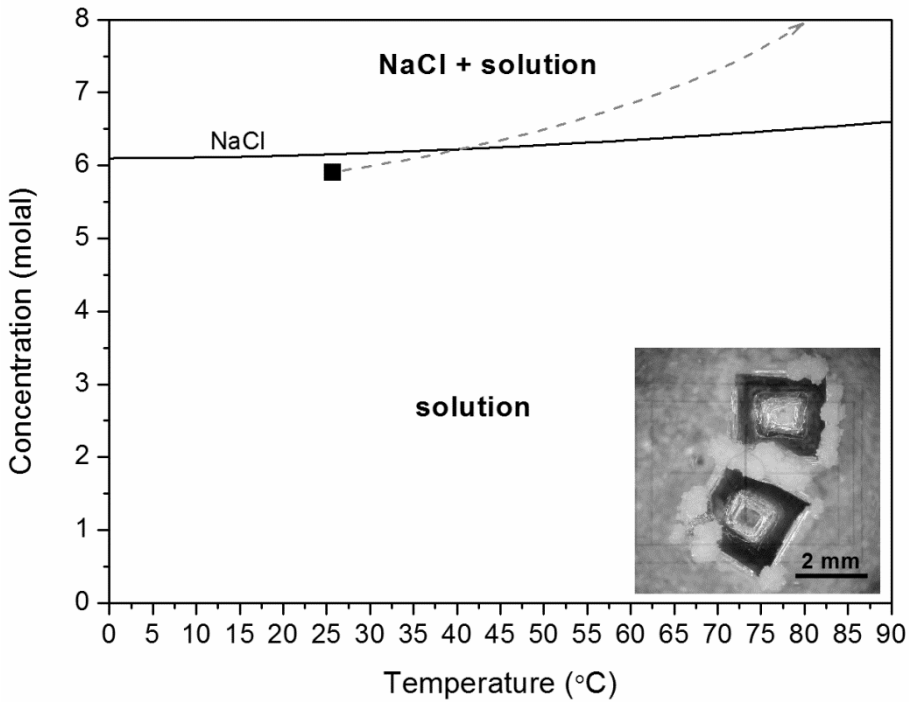

719

720 Figure 5. Solubility diagram of sodium chloride in the temperature range 0 – 90°C [45]:
721 halite, NaCl, anhydrous salt. The cubic crystal structure of halite is represented in the inset
722 figure. The drying process of sample Dc is indicated by the dashed line. The dashed line gives
723 an indication of the possible temperature-concentration evolution.

724

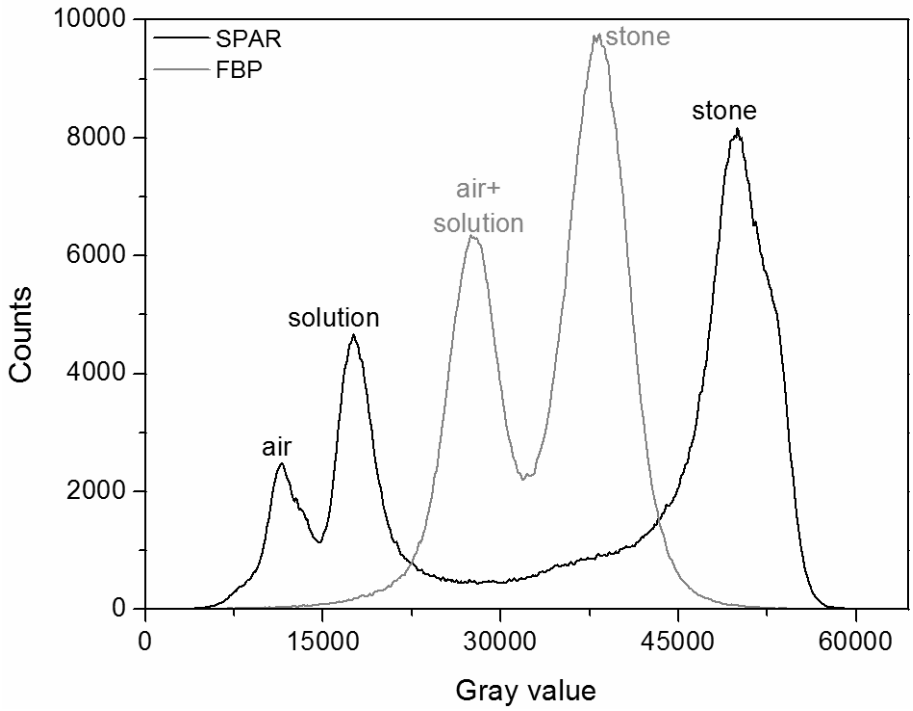

Figure 6. Histogram of sample Ws after a standard filtered backpojection (FBP) reconstruction, based on mixed projection images; and after a reconstruction based on simultaneous phase-and-amplitude retrieval (SPAR).

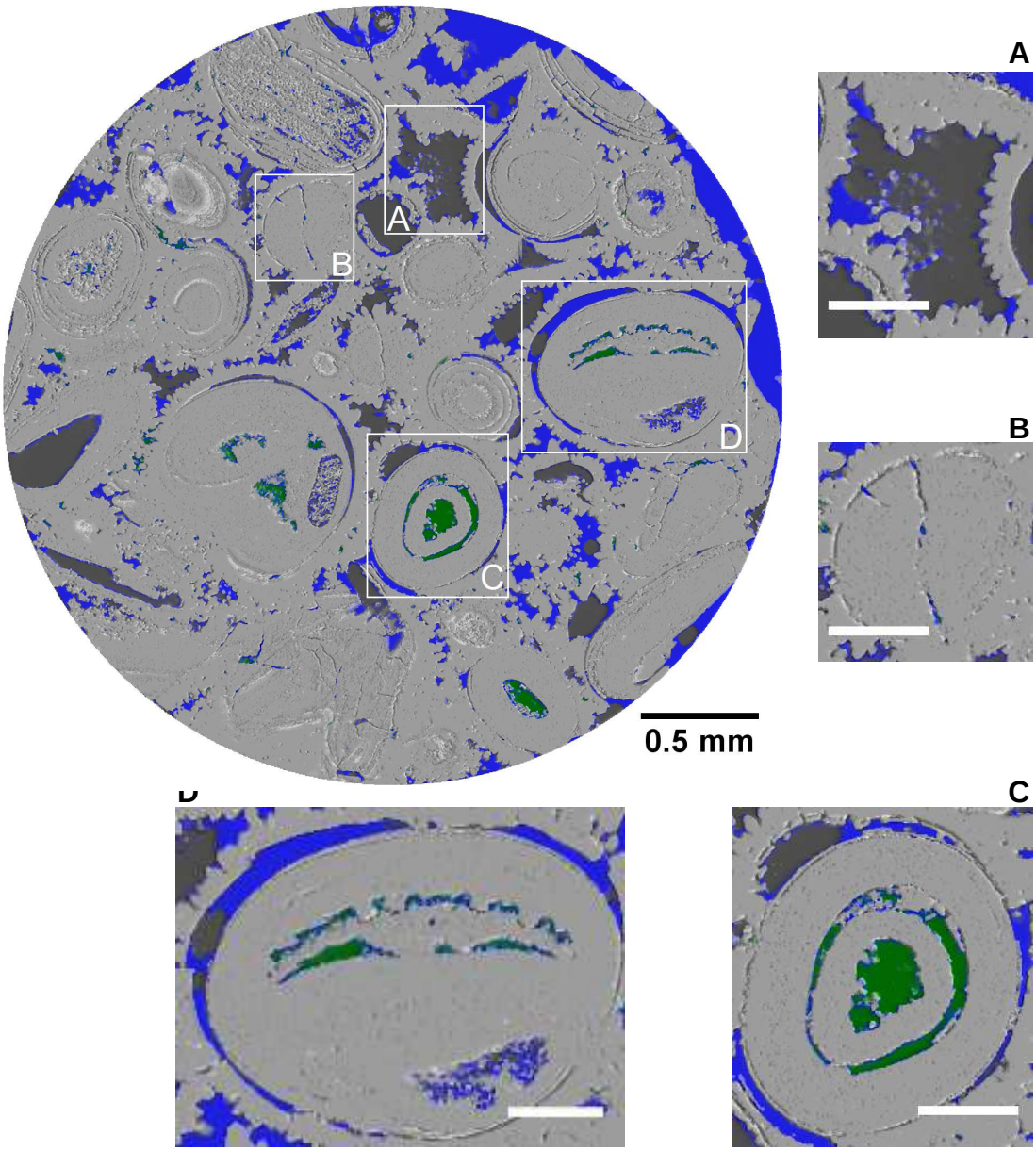

730

731 Figure 7. Horizontal cross section of sample Ws, with the sodium sulfate solution in blue and
732 the not wetted porosity in dark gray and green. Close-ups of the areas marked by the white
733 rectangles are given in the four inset figures. The scale bar in the inset figures represents 0.2
734 mm.

735

(a)

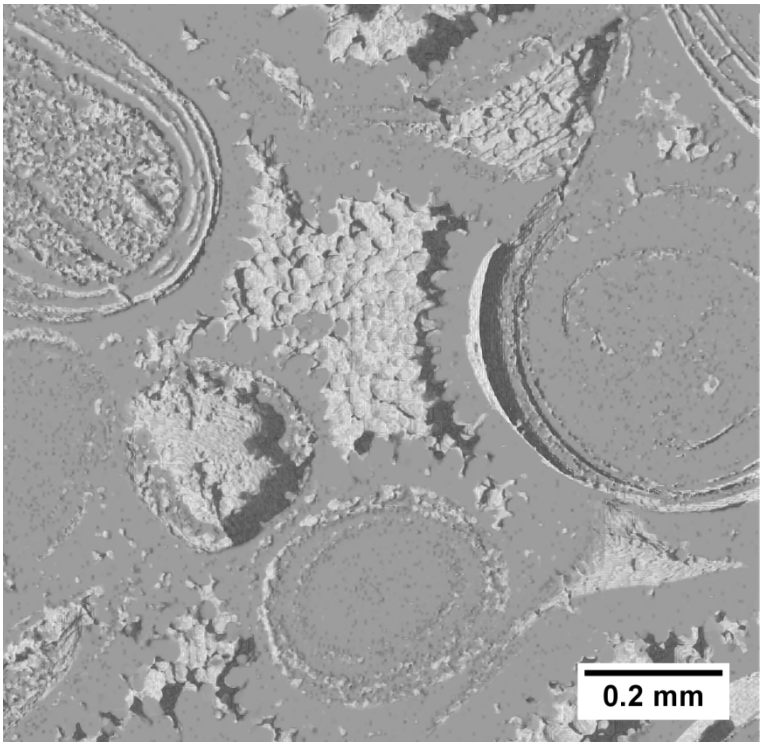

(b)

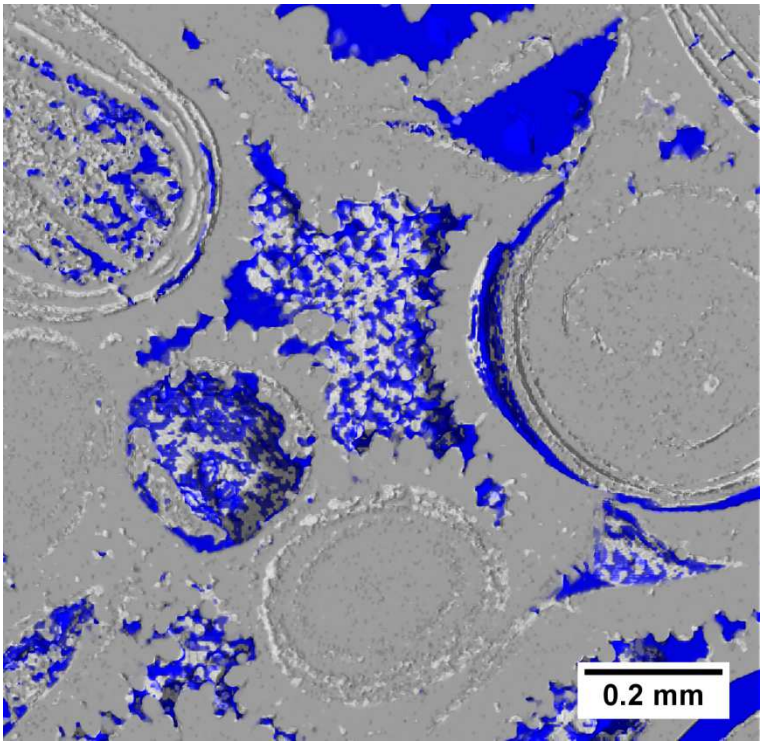

Figure 8. Close-up on the top part of Figure 7 (area A and surrounding), without coloring of the porosity. (a) The calcite grains of the oolitic structure of Savonnières limestone are clearly seen in the initial state. (b) After capillary uptake, the solution forms liquid clusters in between the grains.

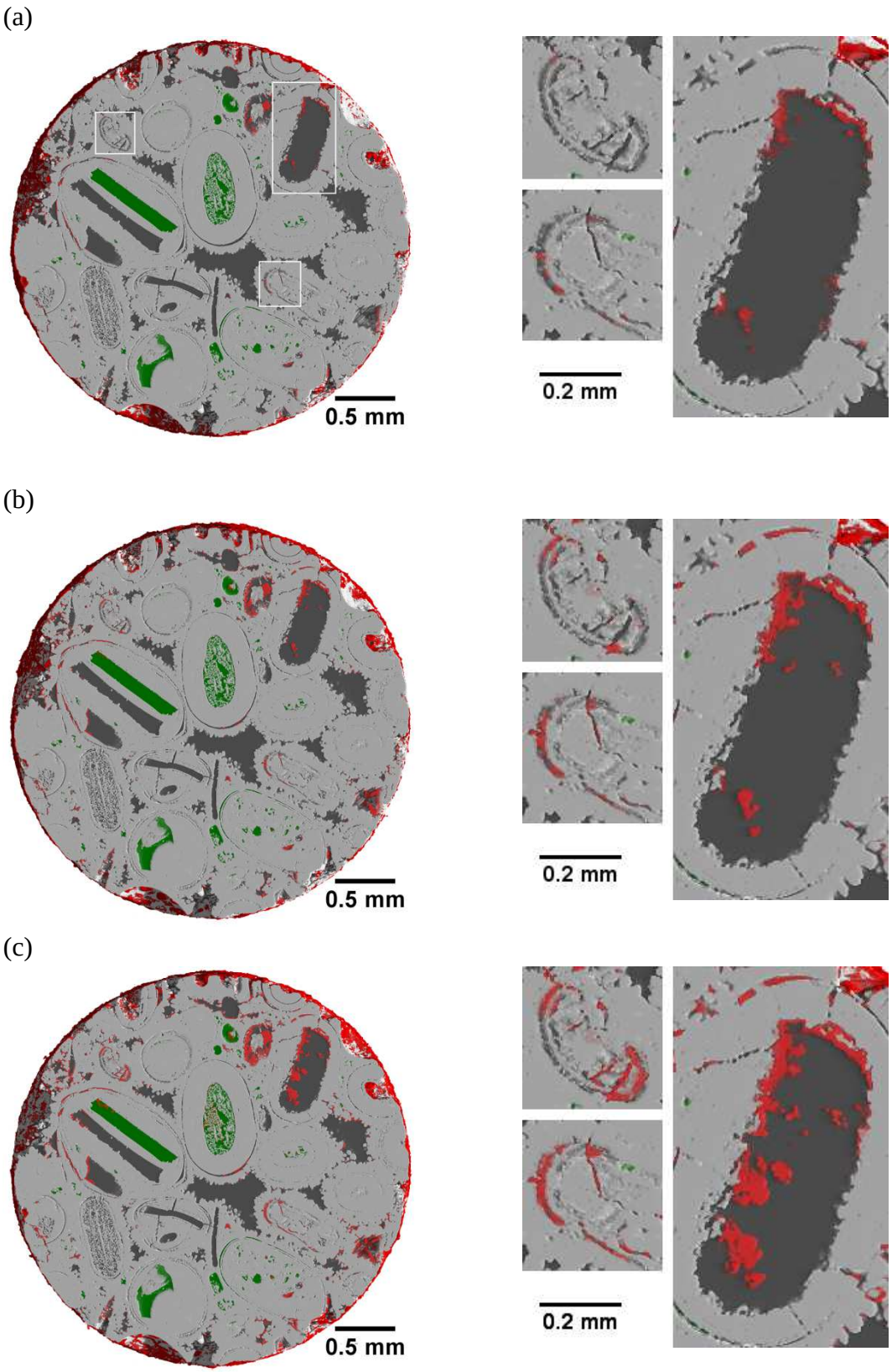

745 Figure 9. Distribution of NaCl crystals, colored in red, in the sample Dc after (a) the first, (b)
746 the second and (c) the third wetting-drying cycle with a 5.8 molal sodium chloride solution.
747 The porosity is represented in dark gray and green. On the right side, a close-up of the areas
748 indicated by the white rectangles in figure (a) is given.

(a) (b)

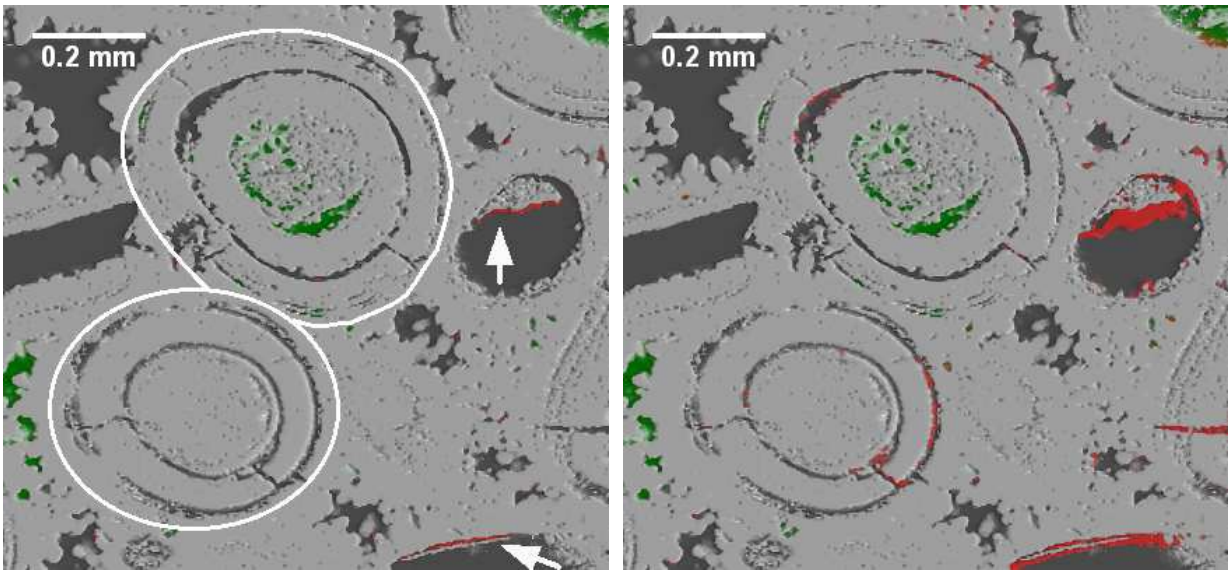

749 Figure 10. Distribution of Na_2SO_4 crystals, colored in red, in a part of the sample Ds after (a)
750 the first and (b) the fourth wetting-drying cycle with a 2.8 molal sodium sulfate solution. The
751 porosity is colored in dark gray and green. In the secondary porosity of hollow oolites
752 (indicated by the white arrows in figure a), a salt crust builds up. In the secondary porosity of
753 detached oolites (white circled in figure a) Na_2SO_4 accumulates.
754

(a)

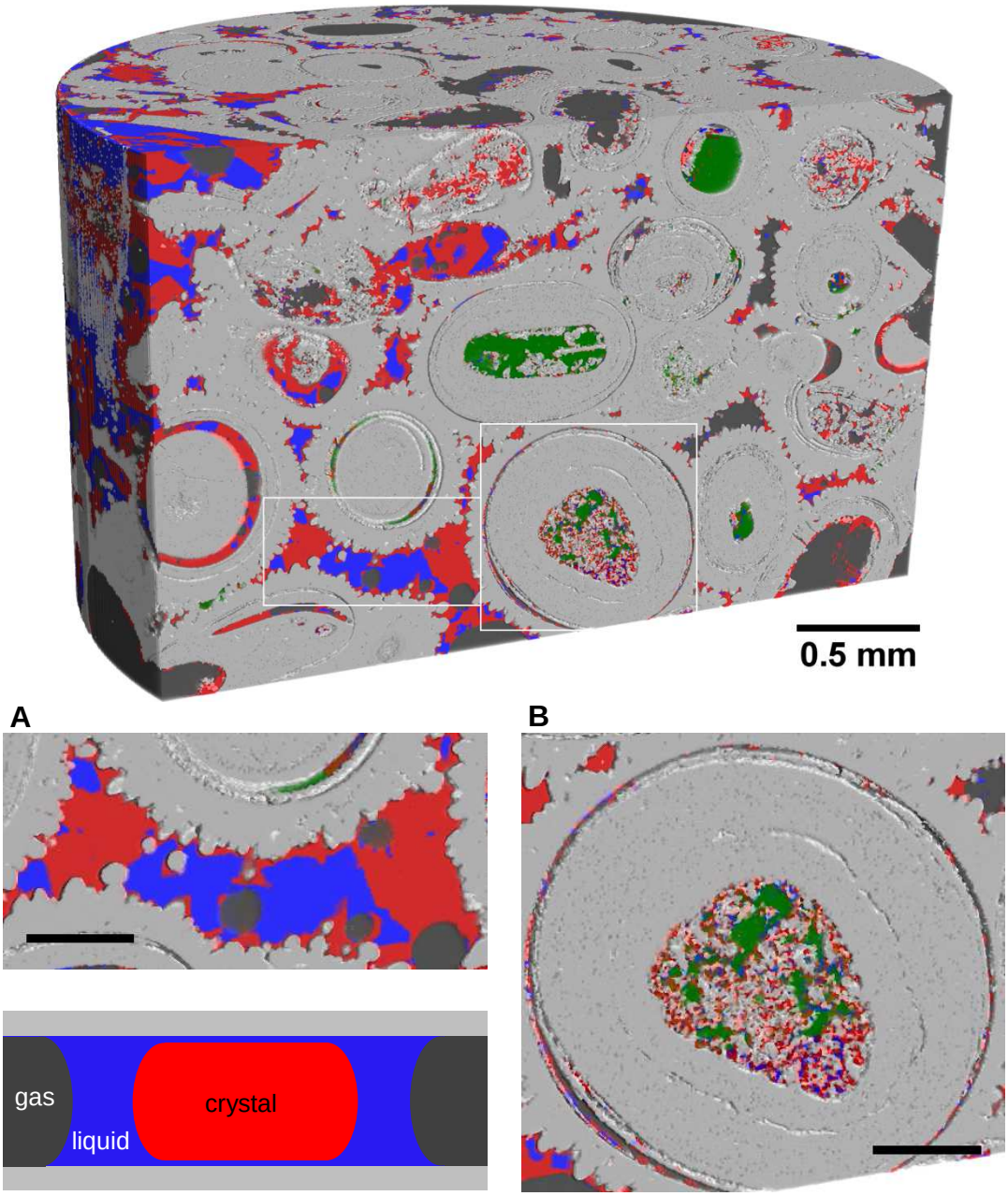

Figure 11. Distribution of hydrated sodium sulfate crystals, in red, and salt solution, in blue, after cooling sample Cs. The not wetted porosity is represented in dark gray and green. Close-ups of the areas marked by the white rectangles are given in the inset figures. Inset A partly resembles the schematic representation from the literature of a crystal in a cylindrical pore (see also Figure 1). The scale bar in the inset figures represents 0.2 mm.

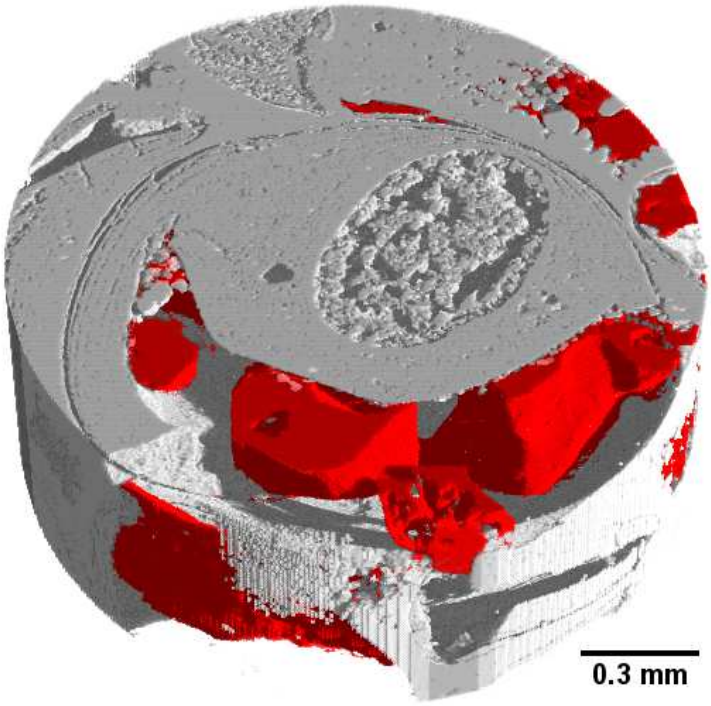

762

763 Figure 12. Close-up of a macropore in sample Cs. The hydrated sodium sulfate crystals are
764 represented in red. The liquid phase and the porosity are not visualized for clarity. The crystal
765 shape suggests that the hydrated crystal is sodium sulfate heptahydrate.

766

(a)

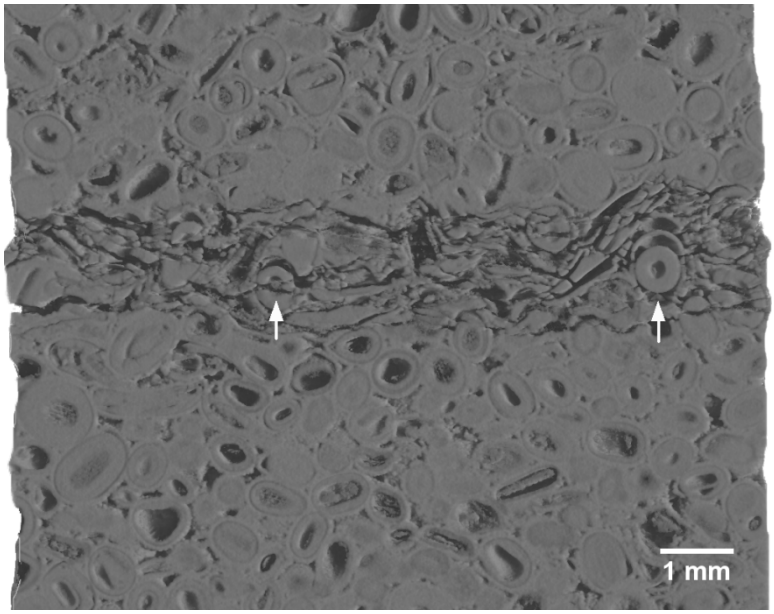

(b)

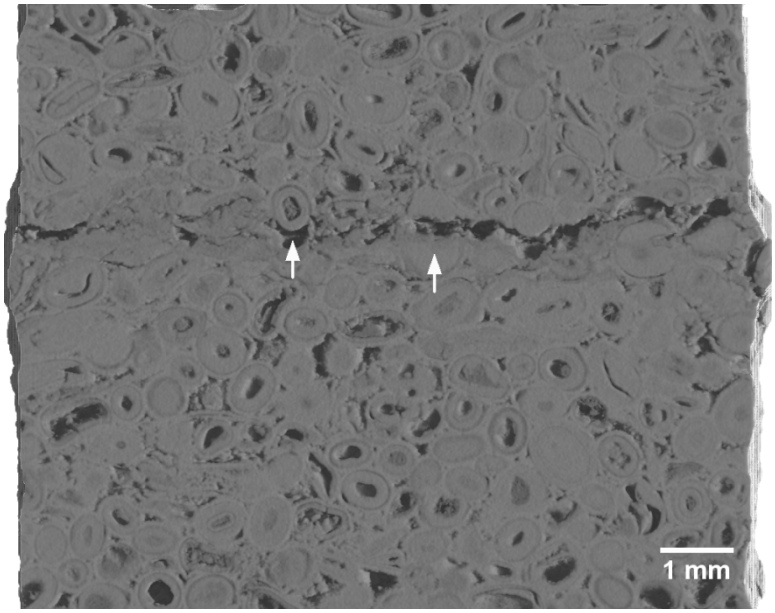

Figure 13. Zoom on the vertical cross section of two Savonnières samples, as described by [38], (a) after 4 wetting-drying cycles with 1.4 molal Na_2SO_4-solution and (b) after 3 wetting-drying cycles with 5.8 molal NaCl-solution. The white arrows point to cracks formed around ooids and through ooids.